Journal of Colloid and Interface Science 544 (2019) 25–36

Contents lists available at ScienceDirect

Journal of Colloid and Interface Science

journal homepage: www.elsevier.com/locate/jcis

Regular Article

$BiO_xCl_y/BiO_mBr_n/BiO_pI_q$/GO quaternary composites: Syntheses and application of visible-light-driven photocatalytic activities

Ciao-Wei Siao [a], Wen-Lian William Lee [b,c], Yong-Ming Dai [a], Wen-Hsin Chung [d], Jiun-Ting Hung [a], Peng-Hao Huang [a], Wan-Yu Lin [d], Chiing-Chang Chen [a,*]

[a] Department of Science Education and Application, National Taichung University of Education 403, Taiwan, ROC
[b] Department of Occupational Safety and Health, Chung-Shan Medical University, Taichung 402, Taiwan, ROC
[c] Department of Occupational Medicine, Chung-Shan Medical University Hospital, Taichung 402, Taiwan, ROC
[d] Department of Plant Pathology, National Chung Hsing University, Taichung 402, Taiwan, ROC

GRAPHICAL ABSTRACT

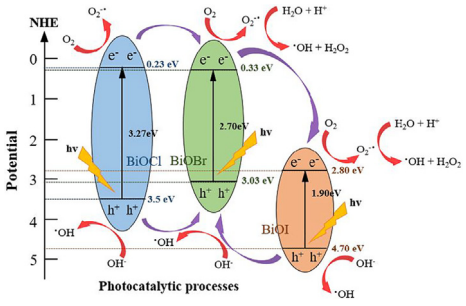

ARTICLE INFO

Article history:
Received 18 January 2019
Accepted 20 February 2019
Available online 21 February 2019

Keywords:
$BiO_xCl_y/BiO_mBr_n/BiO_pI_q$
GO
2-hydroxybenzoic acid
Photocatalytic
Composites

ABSTRACT

Herein, the preparation of numerous bismuth oxychloride/bismuth oxybromide/bismuth oxyiodide/graphene oxide ($BiO_xCl_y/BiO_mBr_n/BiO_pI_q$/GO) composites is reported. A facile hydrothermal method was employed to synthesize these photocatalysts, which had various GO contents. A total of 10 bismuth-oxyhalide composites were isolated and characterized using FE–SEM, XRD, FE–TEM, UV–Vis–DRS, FT–IR, EPR, HR–XPS, PL, and BET. The photocatalytic efficiencies of these 10 bismuth-oxyhalide composites were measured under visible-light irradiation by estimating the concentration of 2-hydroxybenzoic acid (HBA) degradation. The findings indicated that the rate constant order of the HBA degradations was BiOCl/BiOBr/BiOI/GO > $Bi_3O_4Cl/Bi_3O_4Br/Bi_4O_5I_2$/GO > $Bi_{12}O_{17}Cl_2/Bi_3O_4Cl/Bi_{12}O_{17}Br_2/Bi_7O_9I_3$/GO > $Bi_{12}O_{17}Cl_2$/BiOBr/BiOI/GO > $Bi_{12}O_{17}Cl_2/Bi_{12}O_{17}Br_2/Bi_7O_9I_3/Bi_5O_7I$/GO > Bi_3O_4Cl/BiOBr/$Bi_3O_4Br/Bi_4O_5I_2$ > Bi_3O_4Cl/BiOBr/BiOI > BiOCl/BiOBr/BiOI > $Bi_{12}O_{17}Cl_2/Bi_5O_7Br/Bi_5O_7I$ > GO. A maximum rate constant of 0.191 h^{-1} was reached for BiOCl/BiOBr/BiOI/GO, providing photocatalytic efficiency that was eight times higher than that of composite BiOCl/BiOBr/BiOI. We also proposed a photocatalytic mechanism demonstrating that $O_2^{\cdot-}$, $h^{\pm}$, ·OH, and $^1O_2$ are all essential for HBA degradation.

1. Introduction

Recently, much discussion has focused on the use of bismuth-oxyhalide semiconductors in solar cell conversion and environmental remediation. Most notably, after screening 27,000 semiconductor

* Corresponding author.
E-mail address: ccchen@mail.ntcu.edu.tw (C.-C. Chen).

https://doi.org/10.1016/j.jcis.2019.02.067
0021-9797/

materials, research groups at both the University of Cambridge and Massachusetts Institute of Technology selected bismuth oxyiodide (BiOI) as one of the film layers of an all-inorganic solar cell (ITO|NiOx|BiOI|ZnO|Al). The light conversion rate realized using this cell could reach up to 80%, and the strongly enhanced photovoltaic performance was much higher than that of silicon crystal plate (23%) or of lead-based perovskite (21%). BiOI has therefore demonstrated its value as one of the leading candidates for third-generation solar cell materials based on its cost–performance evaluation, nontoxicity, easy availability, stability, and defect tolerance [1,2].

The bioactive plant hormone 2-hydroxybenzoic acid (HBA, named salicylic acid) can be found in several traditional medicines [3]. Pharmacologists have studied HBA and its derivatives in the form of aspirin, which can be given to patients to help avoid and alleviate numerous metabolic disorders [4]. A major concern in recent years has been the discovery that HBA is present at levels of 50 ppm in industrial wastewater, rivers, and civic wastewater systems, which can cause great damage to the environment and human health [5,6]. However, current methods for the treatment of wastewater do not usually remove HBA [7–9]. Advanced oxidation processes (AOPs) have been proposed as a plausible solution [10]. Specifically, photocatalysis is a crucial AOP for consideration in the demolition of low amounts of water-soluble organic pollutants such as HBA [11]. HBA photodegradation has been reported using composite photocatalysts, including BiOX/BiOY (X, Y = Cl, Br, I) [12–16], Fe/CeO_2 [17], $PbBiO_2X$ [18–21], Nanotube-TiO_2 [22], MWCNT/TiO_2 [23], and Al/Fe_2O_3 [24]. However, a cheaper, more efficient method to remove HBA has rarely been reported.

To improve photocatalysis activity, composites can be coupled to modify electronic properties and achieve different morphologies, sizes, and properties of photocatalysts. When in the presence of visible-light illumination, fine tuning the hierarchical architectures of photocatalysts may favor the efficient segregation of photogenerated electron–hole pairs [25]. Bismuth oxyhalides and their composites [12–14,26,27] with layered structures segregate photogenerated electron–hole pairs, and this has been verified to stimulate favorable photocatalytic degradation.

Chen and their research team have studied BiOX (X = Br, I) families [27–30]. A series of binary and ternary bismuth-oxyhalide compounds, namely BiOX/BiOY/BiOZ (X = Cl; Y = Br; Z = I) [12–14,25,31], have been prepared and equipped with unique visible-light driven photocatalytic capabilities to degradate phenol, CV, and HBA. Moreover, bi-phases BiOBr/BiOI composites were prepared, and applications that remove NO are much greater than those that use TiO_2 under visible-light-driven irradiation [32]. Furthermore, Zhang et al. [33] demonstrated that BiOCl/BiOI could be a favorable photocatalytic candidate for degradation of bisphenol under visible light irradiation. Diffuse reflectance spectroscopy (DRS) analysis results revealed that BiOCl/BiOI absorbed visible light to induce electron–hole pair generation and segregation [34].

Graphene (GR), reduced graphene oxide (rGO), graphene oxide (GO), and graphyne are notable for their superior conductivity compared with other two-dimensional (2D) materials and for their unique, 2D configurations, properties that make them excellent electronic mediators [35]. The interfacial contact and high-level adsorption activity of GR serve to make it an ideal support 2D material. Moreover, GR materials have high carrier mobility, and the structure of GR is both strong and flexible. Accordingly, the photocatalysts of composites that have been hybridized with GR, including BiOF/BiOI/GO [13], BiOCl/BiOI/GO [36], and BiOI/GR [37], display excellent photocatalytic efficiency. Such composites can be considered precursors of reactions for growing semiconductor/GR (or GO, rGO) composites by using chemical or thermal processes. Combining GO into a semiconductor was shown by an earlier study to cause improved photocatalytic efficiency [38].

In this paper, we demonstrate a simple method for synthesizing a series of quaternary $BiO_xCl_y/BiO_mBr_n/BiO_pI_q$/GO through a one-step controlled hydrothermal and template-free synthesis. The combination of $BiO_xCl_y/BiO_mBr_n/BiO_pI_q$ and GO is promising because it simultaneously possesses excellent adsorptivity, transparency, conductivity, and controllability. In the photodegradation of HBA, these quaternary composites exhibited much higher removal rates compared with the bare $BiO_xCl_y/BiO_mBr_n/BiO_pI_q$ and other quaternary composites. This study of visible-light-driven reaction pathways also helped clarify possible applications in organic compound degradation and environment remediation.

2. Experiment

2.1. Materials

In this study, we used analytical-grade chemicals, none of which were purified further. In addition, we collected the following reagents: isopropanol (Merck), potassium iodide, *p*-benzoquinone (Alfa Aesar), potassium bromide (Katayama), potassium chloride (Shimakyu), HBA, ammonium oxalate (Osaka), bismuth nitrate, and sodium azide (Sigma). In addition, Merck Co. served as the source for reagent-grade CH_3COONH_4, HNO_3, and NaOH as well as for HPLC-grade CH_3OH.

2.2. Analytical instruments

We acquired X-ray diffraction (XRD) patterns by executing a diffractometer (MAC Science MXP18) administering Cu-Kα irradiation (set conditions: 80 mA and 40 kV). We also employed the X-ray photoelectron spectroscopy (XPS) instrument PHI Quantera SXM (ULVAC-PHI) to collect UV photoelectron spectroscopy data. A Hitachi F-7000 was employed to examine photoluminescence (PL). A JEOL JSM-7401F microscope, exhibiting a 15 kV acceleration voltage, was used for field-emission–scanning electron microscopy–energy dispersive spectroscopy (FE–SEM–EDS). In addition, a 200 kV-acceleration-voltage JEOL-2010 microscope provided EDS spectra and selected-area electron diffraction patterns, in addition to providing field-emission transmission electron microscopy (FE–TEM) images and high-resolution TEM images. We also used an ULVAC-PHI spectrometer, in which we set Al-Kα radiation at 15 kV, for high-resolution XPS (HR–XPS). We applied a Scinco SA-13.1 spectrophotometer at room temperature to record UV–visible DRS (UV–Vis–DRS; λ = 300–800 nm) spectra. We measured chlorine, bromine, and iodine ion concentration in aqueous solution by executing ion chromatography (IC) with a Metrohm instrument (model 883 Basic IC plus ion chromatograph). Sodium carbonate served as the standard eluent, with Metrosep A Supp 5–150 serving as the column. In addition, using a Micromeritics Gemini system, we examined the photocatalysts' Brunauer–Emmett–Teller (BET) specific surface areas (S_{BET}) at 237 °C; in all measurement processes executed at liquid-nitrogen temperature, we employed nitrogen gas as the adsorbate. Finally, we employed an Agilent 5310A frequency counter running in the X band and a Brüker ER200D spectrometer to record electron paramagnetic resonance (EPR) spectra at 77 K.

2.3. Preparation of a series $BiO_xCl_y/BiO_mBr_n/BiO_pI_q$/GO

2.3.1. Synthesis of a $BiO_xCl_y/BiO_mBr_n/BiO_pI_q$

We loaded bismuth nitrate (5 mmol) into a 50-mL flask, followed by adding to the flask 5 mL of 4 M HNO_3 aqueous solution. This mixture was continuously stirred, with the pH value adjusted using 2 M NaOH aqueous solution added dropwise. Following observation of colloid precipitate, we made dropwise additions of

3 M portions of KI, KBr, and KCl (using different molar ratios, KI: KBr:KCl) to the mixture. We subjected the colloid solution to vigorous stirring for a period of 30 min, after which we delivered to a stainless steel autoclave (30 mL) with a Teflon lining. This Teflon-lined autoclave was subsequently put in the oven, subjecting it to 12 h heating to 150–250 °C before being left to cool to room temperature. Subsequently, we filtered the acquired precipitate solid, washed it for ionic species removal using a combination of ethanol and deionized water, and finally dried it overnight at 80 °C. The series of $BiO_xCl_y/BiO_mI_n/BiO_pI_q$ composites was synthesized with controllable reaction conditions (KCl:KBr:KI = 1:1:1, pH = 1–13, hydrothermal times = 12 h, and hydrothermal temperature = 150 °C), as symbolized in Table 1. Samples prepared were marked with symbols named from BC1B1I1-1-150-12 to BC1B1I1-13-150-12 [12].

2.3.2. Synthesis of graphene oxide

GO powders were synthesized by stirring 10 g of $NaNO_3$ and a total of 2 g of powdered flake graphite into a 0 °C ice bath containing 46 mL of H_2SO_4. We added a total of 6 g of potassium permanganate to the suspensions under vigorous stirring. Subsequently, we removed the ice bath to raise the dispersion temperature to 35 °C, where it was maintained overnight. Another 6 g of potassium permanganate was then placed into the suspensions; this was then allowed to stand for 3 h. Later, the glue was slowly stirred with 92 mL of H_2O, which led to intense bubbling and the reaction temperature rising to 95 °C. The color of the dilutions turned brown, and they were maintained for 15 min at this temperature. Subsequently, approximately 280 mL of warm water and 30 wt% H_2O_2 was used to further dilute the suspensions in order to decrease the remaining $HMnO_4$ and MnO_2 and bleach the dissolvable $MnSO_4$. The H_2O_2 treatment caused the suspensions to become shiny yellow solutions. Next, yellow-brown filter cakes were acquired by filtering the suspensions. Once the cakes had been washed with 280 mL of warm water five times, the GO residues were suspended in 200 mL of 10 wt% hydrochloric acid. We executed centrifugation and then overnight oven drying at 60 °C to produce dry GO samples [39].

2.3.3. Synthesis of $BiO_xCl_y/BiO_mBr_n/BiO_pI_q/GO$

We loaded a 50-mL flask with bismuth nitrate (5 mmol), followed by adding 5–50 mg of GO as well as 5 mL of 4 M ethylene glycerol (EG). We also added 2 M sodium hydroxide dropwise while stirring continuously to regulate the pH value; after the formation of a solid precipitate, we also added 2 mL of potassium chloride, potassium bromide, and potassium iodide drop by drop. For 30 min, the aqueous solution was stirred intensely before being placed in a hydrothermal autoclave (30 mL) with a Teflon lining. This was baked for 12 h to 150 °C before being left to slowly cool to room temperature. We first collected the resulting solid precipitates using filtration, followed by cleaning them with CH_3OH and deionized H_2O to withdraw all types of ionic species and finally subjecting them to overnight drying executed at 80 °C. We prepared different $BiO_xCl_y/BiO_mI_n/BiO_pI_q/GO$ samples (Table 1) using the following conditions: molar ratio [Bi $(NO_3)_3{\cdot}5H_2O$/KCl: KBr: KI (1:1:1)], pH value = 1–13, hydrothermal temperature = 150 °C, and hydrothermal time = 12 h. The as-prepared photocatalyst was labeled with symbols arranged from BC1B1I1-1-150-12-0.005gGO to BC1B1I1-13-150-12-0.05gGO.

2.4. Reactions of photocatalytic degradation

In this research, we selected HBA as the object pollutant to examine the efficiency of photocatalytic degradation. Solution suspensions of 100-mL 10 ppm HBA were combined in 100-mL flasks with 10 mg of the photocatalysts. The dispersions' pH values were modified through dropwise addition of NaOH (or HNO_3) aqueous solution. Subsequently, after examining batch adsorption texts, we centrifuged the mixture at 3000 rpm to analyze HBA intensity at a wavelength of 298 nm through UV–Vis absorption spectroscopy. For the implementation of visible-light irradiation, we employed a 420-nm cutoff filter, with irradiations applied by 10-W Xe arc lamps; these lamps were determined to have a set light intensity of 3.51 W/m^2, with a 25-cm distance being between the light and the reaction container. According to set time intervals for irradiation, we took 5-mL aliquots as samples; we then subjected these to centrifugation to remove composited photocatalyst, and we immediately executed UV–Vis spectroscopy to evaluate each supernatant solution.

3. Results and discussion

3.1. Characterization of $BiO_xCl_y/BiO_mI_n/BiO_pI_q/GO$

3.1.1. XRD and TEM

Fig. 1 presents our as-prepared samples' XRD patterns, which indicate the coexistence of various phases. With no GO added to the prepared samples, the fingerprints of ten composites—namely $Bi_4O_5I_2$ [40], BiOI (JCPDS 73-2062), Bi_5O_7I (JCPDS No.40-0548), $Bi_7O_9I_3$ [41], BiOBr (JCPDS No. 09-0393), Bi_3O_4Br (JCPDS No. 84-0793), Bi_5O_7Br (JCPDS No.38-0493), $Bi_{12}O_{17}Br_2$ (JCPDS No. 37-0701), BiOCl (JCPDS No. 85-0861), Bi_3O_4Cl (JCPDS No. 36-0760), and $Bi_{12}O_{17}Cl_2$ (JCPDS No. 37-0702)—are presented in Figs. S1–S4 of the Supplementary Materials [42]. However, with GO added to the prepared samples, the quaternary or even quinary phases in the XRD results were glowing, including BiOCl/BiOBr/BiOI/GO, Bi_3O_4Cl/BiOBr/BiOI/GO, Bi_3O_4Cl/BiOBr/Bi_3O_4Br/BiOI/GO, $Bi_{12}O_{17}Cl_2/Bi_3O_4Br/Bi_4O_5I_2$/GO, and $Bi_{12}O_{17}Cl_2/Bi_5O_7Br/Bi_5O_7I$/GO. The XRD examination results for pH changes of 1, 4, 7, 10, and 13 and GO amounts added are outlined in Table 2.

TEM images reveal that BiOCl/BiOBr/BiOI/GO was composed of various thin sheets of different sizes (Fig. 2a) all containing elemental bismuth, carbon, oxygen, chlorine, bromine, and iodine, as demonstrated in the EDS spectra. The series of photocatalysts contained I, Cl, and Br atomic ratios of nearly 0.50, 5.38, and 3.58, respectively. Furthermore, in agreement with the derived XRD results of the (0 1 2) plane of BiOBr, (1 1 2) plane of BiOI, and (0 0 2) plane of BiOCl, HR–TEM (Fig. 2b) revealed three sets of lattice images corresponding to the following d-spacings: 0.2822, 0.2393, and 0.3645 nm, respectively. This reveals a unique

Table 1
Codes of $BiO_xCl_y/BiO_mBr_n/BiO_pI_q$/GO prepared under different KCl:KBr:KI molar ratio, pH values, and reaction temperatures at 12 h.

pH	GO (g)			
	0	0.005	0.01	0.05
1	BC1B1I1-1-150-12	BC1B1I1-1-150-12-0.005gGO	BC1B1I1-1-150-12-0.01gGO	BC1B1I1-1-150-12-0.05gGO
4	BC1B1I1-4-150-12	BC1B1I1-4-150-12-0.005gGO	BC1B1I1-4-150-12-0.01gGO	BC1B1I1-4-150-12-0.05gGO
7	BC1B1I1-7-150-12	BC1B1I1-7-150-12-0.005gGO	BC1B1I1-7-150-12-0.01gGO	BC1B1I1-7-150-12-0.05gGO
10	BC1B1I1-10-150-12	BC1B1I1-10-150-12-0.005gGO	BC1B1I1-10-150-12-0.01gGO	BC1B1I1-10-150-12-0.05gGO
13	BC1B1I1-13-150-12	BC1B1I1-13-150-12-0.005gGO	BC1B1I1-13-150-12-0.01gGO	BC1B1I1-13-150-12-0.05gGO

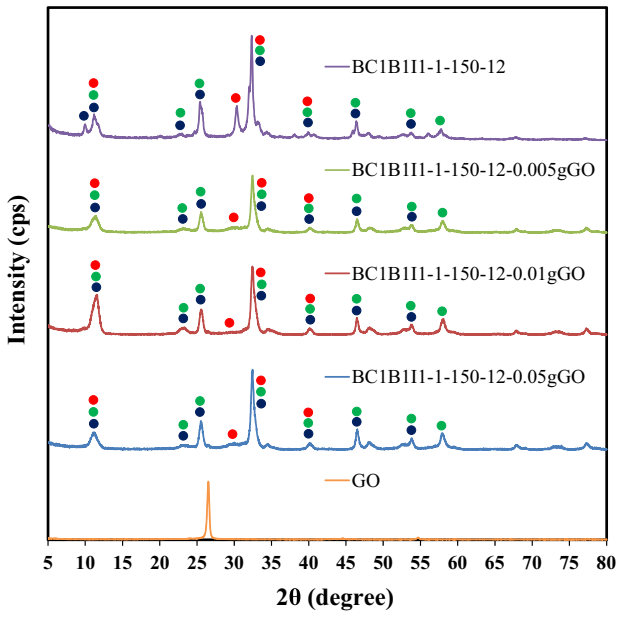

Fig. 1. XRD patterns of as-prepared $BiO_xCl_y/BiO_mBr_n/BiO_pI_q$/GO samples under different amount of GO. (Molar ratio KCl:KBr:KI = 1:1:1, hydrothermal conditions: temp = 150 °C, pH = 1, time = 12 h).

composite, BiOCl/BiOBr/BiOI/GO quaternary phase, prepared using a simple hydrothermal reaction. Notably, at different pH values, the following transformations manifested: $BiOI \rightarrow Bi_4O_5I_2 \rightarrow Bi_7O_9I_3 \rightarrow Bi_3O_4I \rightarrow Bi_5O_7I$, $BiOBr \rightarrow Bi_4O_5Br_2 \rightarrow Bi_3O_4Br \rightarrow Bi_5O_7Br \rightarrow Bi_{12}O_{17}Br_2$ and $BiOCl \rightarrow Bi_4O_5Cl_2 \rightarrow Bi_{24}O_{31}Cl_{10} \rightarrow Bi_3O_4Cl \rightarrow Bi_{12}O_{17}Cl_2$. Some chemical reactions may have caused generation of $BiO_xCl_y/BiO_mBr_n/BiO_pI_q$, as described in Eqns. (1)–(26):

$$2Bi(OH)_{3(s)} + I^- \rightarrow BiOI_{(s)} + H_2O + OH^-{}_{(aq)} \quad (1)$$

$$Bi^{3\pm}{}_{(aq)} + 3\ I^-{}_{(aq)} \rightarrow BiI_{3(s)} \quad (2)$$

$$BiI_{3(s)} + 2\ OH^-{}_{(aq)} \rightarrow BiOI_{(s)} + 2\ I^-{}_{(aq)} + H_2O \quad (3)$$

$$4BiOI_{(s)} + 2\ OH^-{}_{(aq)} \rightarrow Bi_4O_5I_{2(s)} + 2\ I^-{}_{(aq)} + H_2O \quad (4)$$

$$7Bi_4O_5I_{2(s)} + 2\ OH^-{}_{(aq)} \rightarrow 4\ Bi_7O_9I_{3(s)} + 2\ I^-{}_{(aq)} + H_2O \quad (5)$$

$$3Bi_7O_9I_{3(s)} + 2\ OH^-{}_{(aq)} \rightarrow 7\ Bi_3O_4I_{(s)} + 2\ I^-{}_{(aq)} + H_2O \quad (6)$$

$$5Bi_3O_4I_{(s)} + 2\ OH^- \rightarrow 3\ Bi_5O_7I_{(s)} + 2\ I^- + H_2O \quad (7)$$

$$2Bi_5O_7I_{\ (s)} + 2\ OH^-{}_{(aq)} \rightarrow 5\ Bi_2O_{3(s)} + 2\ I^-{}_{(aq)} + H_2O \quad (8)$$

$$2Bi(OH)_{3(s)} + Br^-{}_{(aq)} \rightarrow BiOBr_{(s)} + H_2O + OH^-{}_{(aq)} \quad (9)$$

$$Bi^{3\pm}{}_{(aq)} + 3Br^-{}_{(aq)} \rightarrow BiBr_{3(s)} \quad (10)$$

$$BiBr_{3(s)} + 2OH^-{}_{(aq)} \rightarrow BiOBr_{(s)} + 2Br^-{}_{(aq)} + H_2O \quad (11)$$

$$4BiOBr_{(s)} + 2OH^-{}_{(aq)} \rightarrow Bi_4O_5Br_{2(s)} + 2Br^-{}_{(aq)} + H_2O \quad (12)$$

$$6Bi_4O_5Br_{2(s)} + 2OH^-{}_{(aq)} \rightarrow Bi_{24}O_{31}Br_{10(s)} + 2Br^-{}_{(aq)} + H_2O \quad (13)$$

$$Bi_{24}O_{31}Br_{10(s)} + 2OH^-{}_{(aq)} \rightarrow 8Bi_3O_4Br_{(s)} + 2Br^-{}_{(aq)} + H_2O \quad (14)$$

$$5Bi_3O_4Br_{(s)} + 2OH^-{}_{(aq)} \rightarrow 3Bi_5O_7Br_{(s)} + 2Br^-{}_{(aq)} + H_2O \quad (15)$$

$$12Bi_5O_7Br_{(s)} + 2OH^-{}_{(aq)} \rightarrow 5Bi_{12}O_{17}Br_{2(s)} + 2Br^-{}_{(aq)} + H_2O \quad (16)$$

$$Bi_{12}O_{17}Br_{2(s)} + 2OH^-{}_{(aq)} \rightarrow 6Bi_2O_{3(s)} + 2Br^-{}_{(aq)} + H_2O \quad (17)$$

$$Bi^{3\pm}{}_{(aq)} + 3\ OH^-{}_{(aq)} \rightarrow Bi(OH)_{3(s)} \quad (18)$$

$$Bi(OH)_{3(s)} + 3Cl^-{}_{(aq)} \rightarrow BiCl_{3(s)} + 3\ OH^-{}_{(aq)} \quad (19)$$

$$BiCl_{3(s)} + 2\ OH^-{}_{(aq)} \rightarrow BiOCl_{(s)} + 2Cl^-{}_{(aq)} + H_2O \quad (20)$$

$$4BiOCl_{(s)} + 2\ OH^-{}_{(aq)} \rightarrow Bi_4O_5Cl_{2(s)} + 2Cl^-{}_{(aq)} + H_2O \quad (21)$$

$$6Bi_4O_5Cl_{2(s)} + 2\ OH^-{}_{(aq)} \rightarrow Bi_{24}O_{31}Cl_{10(s)} + 2Cl^-{}_{(aq)} + H_2O \quad (22)$$

$$Bi_{24}O_{31}Cl_{10(s)} + 2\ OH^-{}_{(aq)} \rightarrow 8\ Bi_3O_4Cl_{(s)} + 2Cl^-{}_{(aq)} + H_2O \quad (23)$$

$$5Bi_3O_4Cl_{(s)} + 2\ OH^-{}_{(aq)} \rightarrow 3\ Bi_5O_7Cl_{(s)} + 2Cl^-{}_{(aq)} + H_2O \quad (24)$$

$$12Bi_5O_7Cl_{(s)} + 2\ OH^-{}_{(aq)} \rightarrow 5\ Bi_{12}O_{17}Cl_{2(s)} + 2Cl^-{}_{(aq)} + H_2O \quad (25)$$

$$Bi_{12}O_{17}Cl_{2(s)} + 2\ OH^-{}_{(aq)} \rightarrow 6\ Bi_2O_{3(s)} + 2Cl^-{}_{(aq)} + H_2O \quad (26)$$

In this study, the selective preparations were carefully controlled by the molar ratio, pH value, and reaction time and temperature. The equations demonstrate that X^- ($X^- = I^-$, Br^-, and Cl^-) ions were gradually displaced by OH^- ions. The process of the $BiO_xCl_y/BiO_mBr_n/BiO_pI_q$/GO synthesis can be traced by measuring the decrease in X^- concentrations using IC [25]. The results

Table 2
Crystalline phase changes of $BiO_xCl_y/BiO_mBr_n/BiO_pI_q$/GO nanosheets prepared under different reaction conditions.

pH	GO (g)			
	0	0.005	0.01	0.05
1	●●●	●●●	●●●	●●●
4	◆●●	◆●●	◆●●	◆●●
7	◆●◆◆	◆◆◆	◆●◆◆	◆●◆◆
10	▲◆◆	◆◆▲	▲◆◆★	▲◆■★
13	▲▲▲	▲■★▲	▲■★▲	▲■★▲

●BiOCl ◆Bi_3O_4Cl ▲$Bi_{12}O_{17}Cl_2$ ●BiOBr ◆Bi_3O_4Br ▲Bi_5O_7Br
■$Bi_{12}O_{17}Br_2$ ●BiOI ◆$Bi_4O_5I_2$ ★$Bi_7O_9I_3$ ▲Bi_5O_7I

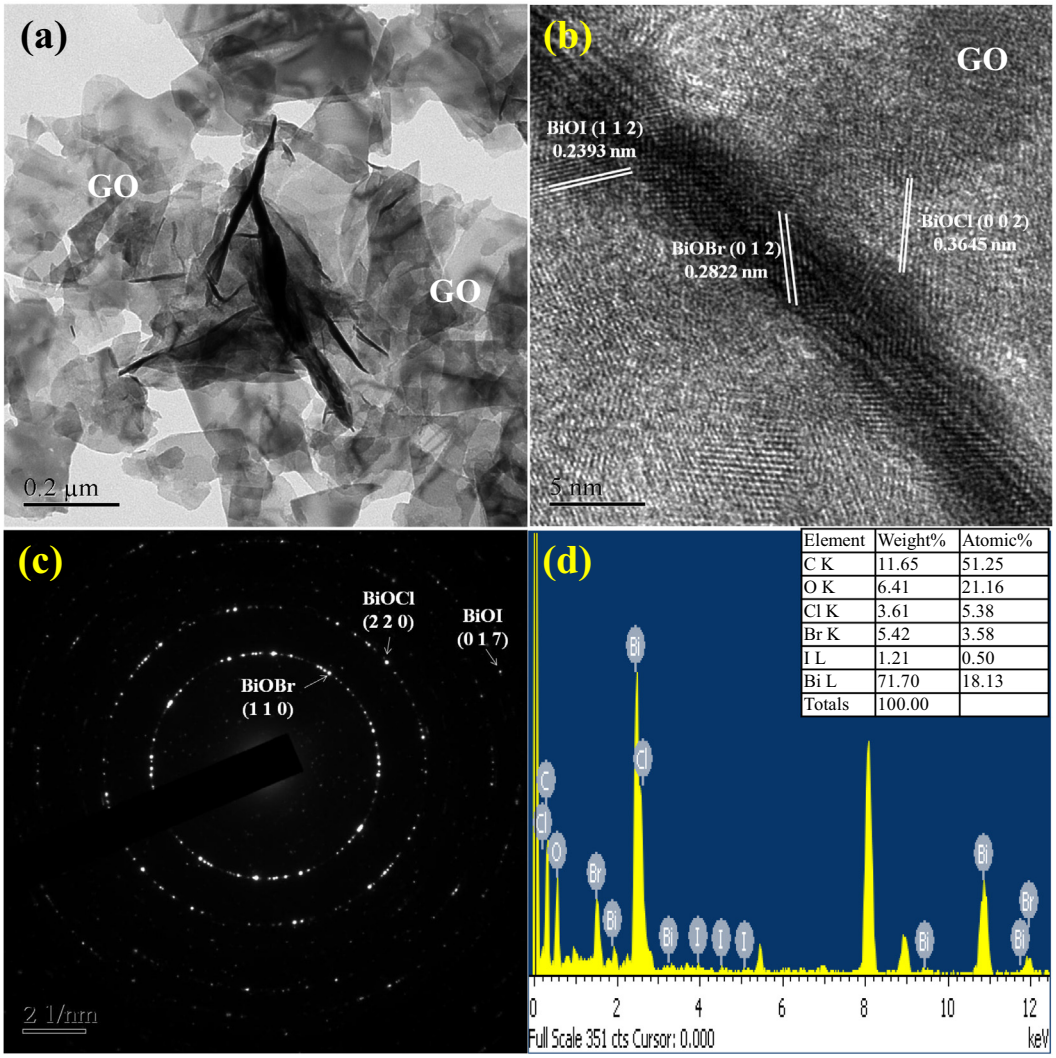

Fig. 2. FE-TEM images and EDS of BC1B1I1-1-150-12-0.005gGO (BiOCl/BiOBr/BiOI/GO) sample by the hydrothermal autoclave method.

demonstrated that as the pH value increased, a series of composites were produced, such as BiOX, $Bi_4O_5X_2$, $Bi_7O_9X_3$, Bi_3O_4X, and Bi_5O_7X (X = I, Br, and Cl). In particular, at pH = 13, α-Bi_2O_3 formed once X^- (X^- = I^-, Br^-, and Cl^-) ions were completely replaced by OH^- ions.

3.1.2. Surface morphology and composition of composite photocatalyst

$BiO_xCl_y/BiO_mBr_n/BiO_pI_q$/GO was prepared through the use of Bi$(NO_3)_3{\cdot}5H_2O$ as well as a KI, KBr, and KCl mixture (molar ratio 1:1:1) by using a hydrothermal autoclave at various pH values. To gain further insight, we executed SEM–EDS to probe the samples' surface morphologies. Figs. 3 and S5–S8 illustrate the various products from the corresponding morphological changes, such as nanosheets, nanoplate crystal shapes, microsheets, irregular thin plates, irregular cluster crystals, and microsheet flower crystals. These photocatalysts were clarified as BiOCl/BiOBr/BiOI/GO, Bi_3O_4-Cl/BiOBr/BiOI/GO, Bi_3O_4Cl/BiOBr/Bi_3O_4Br/$Bi_4O_5I_2$/GO, Bi_3O_4Cl/Bi_3-O_4Br/$Bi_4O_5I_2$/GO, $Bi_{12}O_{17}Cl_2$/Bi_3O_4Br//$Bi_4O_5I_2$/GO, Bi_3O_4Cl/$Bi_{12}O_{17}Cl_2$/Bi_3O_4Br/$Bi_7O_9I_3$/GO, $Bi_{12}O_{17}Cl_2$/Bi_5O_7Br/Bi_5O_7I/GO, and $Bi_{12}O_{17}Cl_2$/$Bi_{12}O_{17}Br_2$/$Bi_7O_9I_3$/Bi_5O_7I/GO composites. In addition, FE–SEM images revealed macroparticle crystals, irregular super-thin sheets, macrothin sheets, microrectangular pillar crystals, and super-thin irregular sheet crystals.

Halogen atoms in the layered structures of bismuth-oxyhalide samples are located among layers of Bi_2O_2, Bi_4O_5, and Bi_6O_8 etc. [43–45]. Researchers considered that the internal electric fields segregating the positive and negative layers (X^-) of $Bi_2O_2^{2+}$, $Bi_4O_5^{2+}$, and $Bi_6O_8^{2+}$ etc. can also efficiently separate photoformed electron–hole pairs, accordingly enhancing the bismuth-oxyhalide photocatalytic efficiency [46]. We found that Bi, Cl, Br, I, C, and O were the six major elements involved with the various pH values, as illustrated in Table 3 and Fig. 2d. For the photocatalysts, the estimated atomic ratios (%) of I (or Br, Cl) were within 0.38–8.11 (or 0.11–10.52, 0.26–11.27), and these values were ascribed to BiOI, $Bi_4O_5I_2$, $Bi_7O_9I_3$, Bi_3O_4I, Bi_5O_7I (or BiOX, $Bi_4O_5X_2$, $Bi_{24}O_{31}X_{10}$, Bi_3O_4X, Bi_5O_7X, $Bi_{12}O_{17}X_2$; X = Br, Cl) and their mixture phase composites, which contrasted with their stoichiometric ratios (Bi:I = 1:1, 2:1, 7:3, 3:1, and 5:1, respectively; Bi:X = 1:1, 2:1, 24:10, 3:1, 5:1, and 6:1, respectively); the designated photocatalysts can be achieved controllably and selectively through a sample hydrothermal autoclave method.

Bismuth oxyhalides with a stoichiometry ratio (Bi:O:X = 1:1:1; X = Cl, Br, I) have a special structure with a tetragonal space group (*P4/nmm*) [43,44]. The three BiOX composites divide the layered structure, in which a positive charge of layer $[Bi_2O_2]^{2+}$ is balanced for a negative charge of layer X^-. Each bismuth atom is encircled by four oxygen and halogen atoms, and this creates an asymmetric

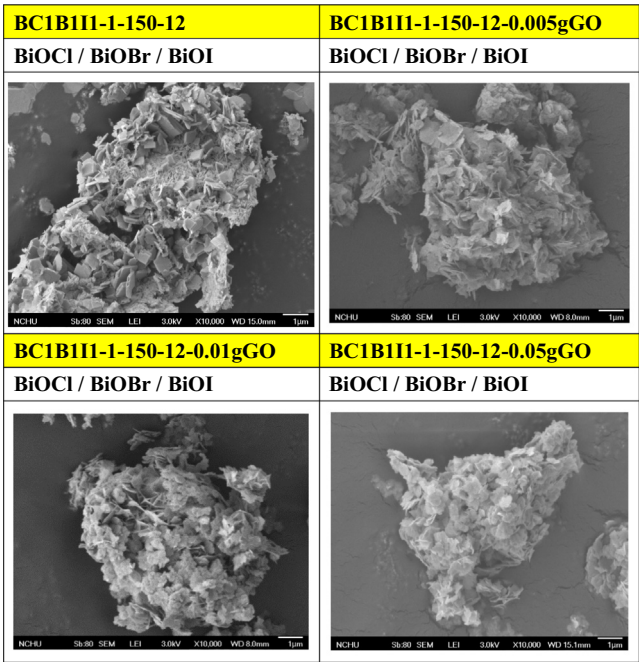

Fig. 3. SEM images of BiOCl/BiOBr/BiOI/GO prepared by the hydrothermal autoclave method under different amount of GO. (Molar ratio KCl:KBr:KI = 1:1:1, hydrothermal conditions: temp = 150 °C, pH = 1, time = 12 h).

decahedron linked in [X—Bi—O—Bi—O—X] bonding that is maintained collectively through van der Waals forces. In the series of X, the lattice parameter *c* grows from 62.3 to 91.5 pm (approximately 46%) due to the expansion of the ionic radius of the X atom, and the lattice parameter *a* grows from 37.5 to 40.9 pm (only 9%) [44,47,48]. The thermal decomposition of BiOX produces the monoclinic structure $Bi_4O_5X_2$ (Bi:X = 2:1 ratio, X = Br, I) [49,50]. The $[Bi_4O_5]^{2\pm}$ (=$[Bi_2O_2]^{2+}$ + Bi_2O_3) layers are segregated by X^- layers. Other similarly associated structures are Bi_3O_4I and Bi_3O_4Br, α-Bi_5O_7I and Bi_5O_7Br, and $Bi_{24}O_{31}Br_{10}$ and $Bi_{24}O_{31}Cl_{10}$ [51–53]. However, β-Bi_5O_7I, $Bi_7O_9I_3$, $Bi_{12}O_{17}Cl_2$, $Bi_{12}O_{17}Br_2$, $Bi_{12}O_{16}Cl_4$, and $Bi_7O_5F_{11}$ share more irregular (less layered) structures [51–53]. In the other structure family, the $[Bi_6O_8]^{2\pm}$ (=$[Bi_2O_2]^{2+}$ + $2Bi_2O_3$), $[Bi_8O_{11}]^{2\pm}$ (=$[Bi_2O_2]^{2+}$ + $3Bi_2O_3$), $[Bi_{10}O_{14}]^{2\pm}$ (=$[Bi_2O_2]^{2+}$ + $4Bi_2O_3$), and $[Bi_{12}O_{17}]^{2\pm}$ (=$[Bi_2O_2]^{2+}$ + $5Bi_2O_3$) layers and Bi_2O_3 are all segregated from each other by X^- layers. The results suggest that gradual insertion of Bi_2O_3 to the positive layers through increasing pH values results in layered structure change following the proposed sequence: $[Bi_2O_2]^{2+}X_2^- \rightarrow [Bi_4O_5]^{2+}\ X_2^- \rightarrow [Bi_6O_8]^{2+}\ X_2^- \rightarrow [Bi_8O_{11}]^{2+}\ X_2^- \rightarrow [Bi_{10}O_{14}]^{2+}\ X_2^- \rightarrow [Bi_{12}O_{17}]^{2+}\ X_2^- \rightarrow Bi_2O_3$.

3.1.3. HR–XPS measurement

The XPS measurement demonstrated that the as-prepared photocatalysts were composed of O 1s, Br 3d, I 3d, Cl 2p, Bi 4f, and C 1s (Fig. 4a). According to Fig. 4b, the characteristic binding energy (E_b) determined for Bi $4f_{7/2}$ was 158.4 eV, which indicated a Bi^{+3} oxidation state. The photocatalysts also exhibited an extra spin–orbit doublet, and the corresponding E_b value determined for Bi $4f_{7/2}$ was 156.5 eV, which suggested partial reduction of Bi caused by the lower valence state. It has been reported by Chen et al. [25,31] that $Bi^{(+3-x)}$ can be attributed to substoichiometric types of Bi, and within the Bi $4f_{7/2}$, there was a chemical shift of 1.5–2.6 eV. Within the Bi_2O_2 layer, there was a trivalent oxidation state of the bond Bi^{+3}—O accompanied by an additional two spin–orbit doublets with the E_b for Bi $4f_{7/2}$ s [25,31]. The HR–XPS spectra displayed in Fig. 4c reveal that three peaks can be resolved for the O 1s region. The peak at 529.7 eV can be determined to be a result of bonds between O and Bi in the $Bi_2O_2^{2+}$ slabs. In addition, the secondary peak (530.6 eV) can be determined to be a result of surface-dwelling hydroxyl groups, and the ternary peak (531.4 eV) can be determined to be a result of the C—O bond [25].

As shown in Fig. 4d, the E_b value determined for Cl $2p_{1/2}$ was 199.3 eV and that determined for Cl $2p_{3/2}$ was 197.6 eV; these results correspond to the appearance of Cl during the monovalent oxidation state. As shown in Fig. 4e, 68.9 eV was the E_b for Br $3d_{3/2}$ and 67.8 eV was that for Br $3d_{5/2}$; these results agree with the monovalent oxidation state of Br. From Fig. 4f, the E_b value determined for I $3d_{3/2}$ was 629.3 eV and that determined for I $3d_{5/2}$ was 619.4 eV, agreeing with the monovalent oxidation state of I. Furthermore, Fig. 4g reveals C 1s in unoxidized states (sp^2 carbon) with three chemically shifted components, namely aromatic rings (284.0 eV), carbonyl groups (C=O, 288.3 eV), and oxygen bonds (C—O, 287.4 eV) [54]. Additionally, the calculated O, Bi, Cl, Br, I,

Table 3
Physical and chemical properties of $BiO_xCl_y/BiO_mBr_n/BiO_pI_q$/GO.

Catalyst code	EDS of atomic ratio(%)						Eg (eV)
	Bi	O	Cl	Br	I	C	
BC1B1I1-1-150-12	28.37	46.66	11.27	10.52	3.18	–	1.92
BC1B1I1-1-150-12-0.005gGO	20.01	36.48	3.04	5.25	2.03	33.19	2.54
BC1B1I1-1-150-12-0.01gGO	17.07	27.07	7.88	6.33	0.38	41.27	2.50
BC1B1I1-1-150-12-0.05gGO	16.06	21.38	6.22	4.85	0.59	50.91	2.27
BC1B1I1-4-150-12	28.56	50.28	5.42	7.63	8.11	–	2.21
BC1B1I1-4-150-12-0.005gGO	19.63	37.55	3.18	4.31	1.47	33.86	2.38
BC1B1I1-4-150-12-0.01gGO	16.43	33.32	3.10	3.95	1.82	41.37	2.40
BC1B1I1-4-150-12-0.05gGO	10.09	20.48	1.94	2.26	0.94	64.28	2.18
BC1B1I1-7-150-12	33.64	49.31	6.49	5.80	4.76	–	2.26
BC1B1I1-7-150-12-0.005gGO	24.49	35.67	3.32	4.16	2.09	30.26	2.29
BC1B1I1-7-150-12-0.01gGO	13.05	40.62	0.53	2.71	1.19	42.44	2.23
BC1B1I1-7-150-12-0.05gGO	14.52	30.88	1.41	3.26	1.61	48.32	2.20
BC1B1I1-10-150-12	24.66	63.66	2.04	3.39	6.26	–	2.43
BC1B1I1-10-150-12-0.005gGO	17.73	41.76	1.20	2.52	1.62	35.17	2.30
BC1B1I1-10-150-12-0.01gGO	13.19	37.33	0.57	–	0.94	47.97	2.31
BC1B1I1-10-150-12-0.05gGO	8.25	29.76	1.00	1.39	0.59	59.01	2.14
BC1B1I1-13-150-12	36.19	57.82	–	–	5.99	–	2.94
BC1B1I1-13–150-12-0.005gGO	19.45	32.64	1.02	–	1.23	45.66	2.67
BC1B1I1-13-150-12-0.01gGO	20.24	21.70	7.82	5.68	0.86	43.70	2.50
BC1B1I1-13-150-12-0.05gGO	13.75	41.50	0.26	0.11	1.06	43.31	2.44

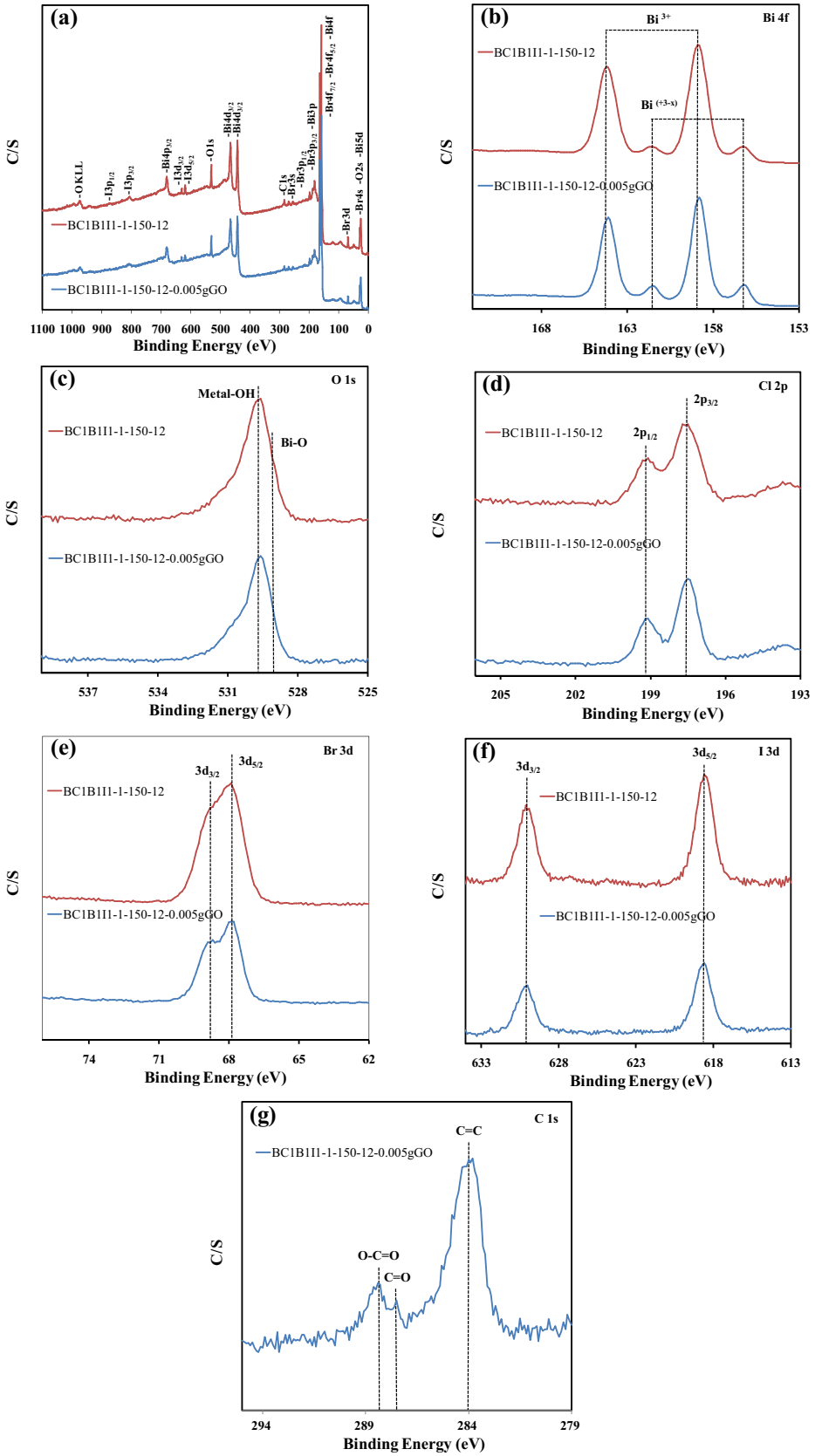

Fig. 4. High resolution XPS spectra of as-prepared BiOCl/BiOBr/BiOI and BiOCl/BiOBr/BiOI/GO samples. (a) total survey; (b) Bi 4f; (c) O 1s; (d) Cl 2p; (e) Br 3d; (f) I 3d; (g) C 1s. (Molar ratio KCl:KBr:KI = 1:1:1, hydrothermal temp = 150 °C, pH = 1, hydrothermal time = 12 h).

and C atomic ratios for the sample were 31.1, 33.1, 8.8, 7.4, 0.9, and 18.7 (%), respectively, which corresponded to the BiOCl/BiOBr/BiOI/GO composite. According to the XPS results, the findings agree with the acquired results from the XRD and HR–TEM analysis

3.1.4. UV–Vis–DRS analysis

Figs. 5 and S9–S12 present the samples' collected UV–Vis–DRS spectra. The quantity of visible light absorbed by both BiOBr and BiOCl was negligible; however, BiOI exhibited strong absorption in the visible area. Moreover, a monotonic red-shift response of bismuth oxychloride was observed for the bismuth oxyiodide absorption edges. Absorption spectra of semiconductors given their energy gap (E_g) values are estimable from the description equation $\alpha h\nu = A(h\nu - E_g)^{n/2}$, where the BiOX n values are 4 [31,55]. According to Figs. 5 and S9–S12, the relationship of $(\alpha h\nu)^{1/2}$ versus energy ($h\nu$) revealed the E_g value of BiOCl/BiOBr/BiOI/GO, and it was determined to range between 2.18 and 2.40 eV. The transitions for the intrinsic band gap existing between the conduction band (C_b) and valence band (V_b), instead of impurity-level-induced transitions, could describe the strong absorption and steep shape occurring in the region of visible light [56].

3.1.5. BET specific surface areas (S_{BET}) of composite photocatalysts

Fig. 6 displays the curves of the N_2 adsorption–desorption isotherms that were examined for BiOCl/BiOBr/BiOI/GO. All isotherm curves of composite photocatalysts were examined to approach the Type IV isotherms specified by the International Union of Pure and Applied Chemistry and were noted to be accompanied by a hysteresis loop that was observed at a pressure from 0.05 to 1.0 [26]. We determined that the shape of the hysteresis loop matched the shape of Type H3, indicating that the composite photocatalysts looked like nanosheets or nanoplates gathered to form pores that were slit-like. The observed agglomeration of the composite photocatalyst was in accordance with a nanosheet-like morphology (Fig. 3) [26] as well as with the FE-SEM images that showed hierarchical 3D structures self-assembled from nanoplates or nanosheets. The contrasting pore size distribution (PSD) curves obtained for BiOCl/BiOBr/BiOI/GO are illustrated in the inset of Fig. 6. For the BiOCl/BiOBr/BiOI/GO composite, the PSD curves are

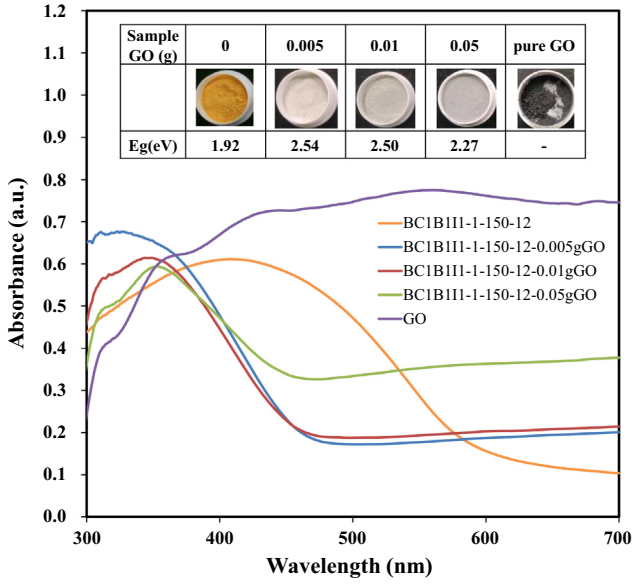

Fig. 5. UV–vis absorption spectra of as-prepared BiOCl/BiOBr/BiOI/GO samples under different amount of GO. (Molar ratio KCl:KBr:KI = 1:1:1, hydrothermal conditions: temp = 150 °C, pH = 1, time = 12 h).

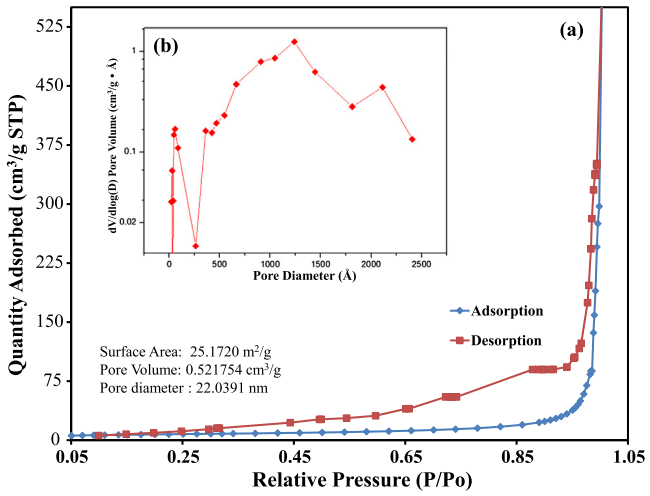

Fig. 6. N_2 adsorption-desorption isotherm distribution curves for enlarged view and the pore distribution curves (inset) of as-prepared of BiOCl/BiOBr/BiOI/GO. (Molar ratio KCl:KBr:KI = 1:1:1, hydrothermal conditions: temp = 150 °C, pH = 1, time = 12 h).

tri-modal, displaying the presence of small (2–4 nm) and medium (10–50 nm) mesopores along with large (50–1100 nm) macropores. In this study, the nanosheets or nanoplates did not contain pores that are visible in Figs. 3 and S5–S8, but the smaller mesopores may indicate that porosity came from the nanosheets or nanoplates. By contrast, the medium mesopores can be attributed to pore progression between the piled nanosheets or nanoplates, and the large macropores can be attributed to the pores produced between the nanosheets or nanoplates. In photocatalysis, such porous, self-assembled architectures have an unusual usability in that they can supply transportation paths for product and reactant molecules [57]. The size and volume of the composite pores were recorded as 0.52 $cm^3\ g^{-1}$ and 22.04 nm, respectively.

The BET isotherm curve of BiOCl/BiOBr/BiOI/GO was used to determine the S_{BET} value, which was approximately 25.17 $m^2\ g^{-1}$. A large pore volume and S_{BET} are related to a large quantity of surface active sites, and they facilitate reactant transport, thereby tending to improve the efficiency of photocatalysis. The high efficiency of the photocatalyst may be attributed to the great S_{BET} and pore volume acquired for BiOCl/BiOBr/BiOI/GO. The nanosheet and nanoplate structure offers pathways that are highly efficient for transporting reactants as well as many active sites for completing the processes of photocatalysis. This results in more efficient yield of photoenergy as well as separation of electron–hole pairs, which ultimately engenders improved photocatalytic performance.

3.2. Activity of photocatalyst

Fig. 7 shows changes in the UV–Vis spectra examined during the photodegradation of HBA in aqueous BiOCl/BiOBr/BiOI/GO suspensions under visible-light irradiation. Approximately 95% of the HBA had degraded after being irradiated for 12 h.

We probed the photodegradation process efficiency as a function of the irradiation time (Figs. 8 and S13–S16). Using BiOCl/BiOBr/BiOI/GO caused photocatalytic activity to markedly improve. After 24 h of irradiation, the BiOCl/BiOBr/BiOI/GO photocatalyst exhibited high-level photocatalytic activity, with photocatalytic efficiency examined for HBA approaching 99.9%. To further understand the reaction kinetics that were underlying the HBA photocatalytic degradation, we utilized a pseudo-first-order model, which is outlined as follows [31]: $\ln(C_o/C) = kt$. We applied a linear fit of the first order to the data presented in Table 4; thus, for photocatalytic

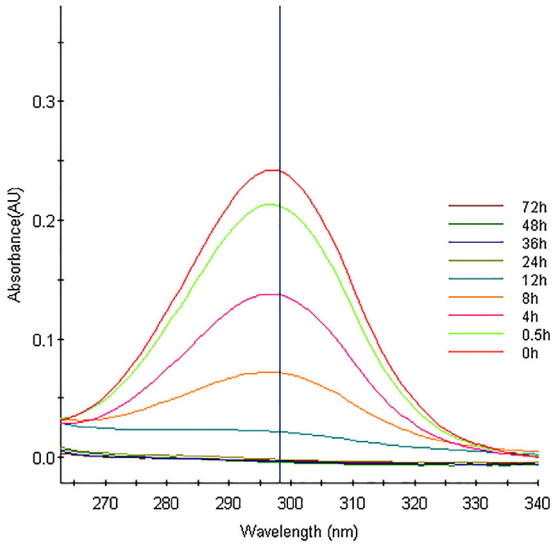

Fig. 7. Temporal UV–vis adsorption spectral changes during the photocatalytic degradation of HBA over aqueous BiOCl/BiOBr/BiOI/GO under visible light irradiation.

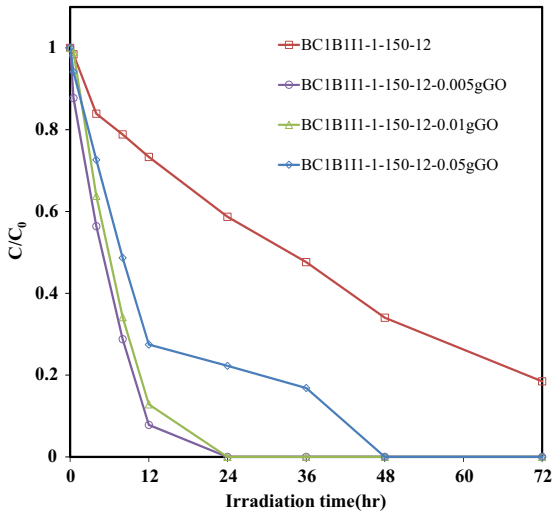

Fig. 8. Photodegradation of HBA as a function of irradiation time over different BiOCl/BiOBr/BiOI/GO photocatalysts. (Molar ratio KCl:KBr:KI = 1:1:1, hydrothermal conditions: temp = 150 °C, pH = 1, time = 12 h).

degradation of HBA, the maximum k value derived for BiOCl/BiOBr/BiOI/GO was 1.91 × 10^{-1} h^{-1}. This rate constant was determined to be superior to that of other composites in the present study, demonstrating that BiOCl/BiOBr/BiOI/GO had the best activity for photocatalytic degradation of HBA.

Table 4 presents a list of multinary bismuth oxyhalides, showing that among the composites in this study, BiOCl/BiOBr/BiOI/GO presented the best photocatalytic efficiency of HBA; furthermore, these experimental results demonstrate photocatalytic performance changes associated with $BiO_xCl_y/BiO_mBr_n/BiO_pI_q$/GO. The improvement in removal efficiency for $BiO_xCl_y/BiO_mBr_n/BiO_pI_q$/GO may be attributed to the layered structure's synergistic effect, heterojunction generation, high surface area S_{BET}, and low-energy band gap. HBA cannot be decomposed without the presence of photocatalysts under visible-light irradiation; hence, the relatively high performance of $BiO_xCl_y/BiO_mBr_n/BiO_pI_q$/GO as a photocatalyst may be because it can efficiently use visible light and can effectively segregate electron–hole pairs existing in $BiO_xCl_y/BiO_mBr_n/BiO_pI_q$/GO heterojunctions.

We recycled BiOCl/BiOBr/BiOI/GO to demonstrate that it is an effectively enduring photocatalyst. We executed centrifugation processes to ensure that we could collect the photocatalyst after each cycle. As shown in Fig. 9a, the removal efficiency of HBA in the fifth cycle exhibited no evident performance loss; even in the fifth cycle, the performance of the photocatalyst decreased by only 4.25%. As illustrated in Fig. 9b, the recycled BiOCl/BiOBr/BiOI/GO was also measured by XRD; no apparent differences were detectable between the reused and as-synthesized composites; accordingly, the photocatalytic stability of BiOCl/BiOBr/BiOI/GO is favorable.

3.3. Pathways of photodegradation of HBA

In the current study, extremely minor changes in HBA concentrations were detectable in blank experiments executed before the photocatalytic reactions. We propose that there is no involvement of the photosensitization mechanism in HBA degradation and that photocatalytic activity mainly depends on the lifetime of photo-induced electron–hole pairs or the recombination rate. Thus, we subjected the derived photocatalyst to PL) spectroscopy to measure the photo-induced electron–hole pairs' recombination rate (Fig. 10). The composite photocatalyst exhibited a weak emission peak at 475–500 nm, probably due to the direct electron–hole recombination of band transitions. We noted BiOCl/BiOBr/BiOI/GO to exhibit a distinctive emission peak at 475–500 nm (the lowest intensity), demonstrating repressed recombination of photoformatted charge carriers. By contrast, efficient separation may lengthen the lifespan of charge carriers and strengthen the interfacial charge transfer effectiveness to the adsorbed photocatalysts, thereby increasing the efficiency of the photocatalysts [25]. The relative intensities of PL that we noted for BiOCl/BiOBr/BiOI/GO were comparatively low, as illustrated in Fig. 10. As presented in Fig. 8 and Table 4, we noted a poor electron–hole recombination rate, a phenomenon that also engendered better photocatalytic performance.

Reactive species, especially $O_2^{\cdot-}$, $HO^{\cdot}$, $H^{\cdot}$, $^1O_2$, and $h^{\pm}$, can be observed in the photocatalytic reaction under visible or UV light irradiation [34,58–60]. Zhang et al. revealed a mechanism for

Table 4
The pseudo-first-order rate constants for the degradation of HBA with $BiO_xCl_y/BiO_mBr_n/BiO_pI_q$/GO photocatalysts under visible light irradiation.

pH	GO (g)							
	0		0.005		0.01		0.05	
	$k(h^{-1})$	R^2	$k(h^{-1})$	R^2	$k(h^{-1})$	R^2	$k(h^{-1})$	R^2
1	0.024	0.946	0.191	0.958	0.156	0.967	0.101	0.981
4	0.073	0.952	0.053	0.984	0.076	0.980	0.064	0.984
7	0.076	0.952	0.098	0.941	0.047	0.920	0.061	0.905
10	0.178	0.951	0.020	0.823	0.087	0.831	0.088	0.827
13	0.005	0.982	0.073	0.926	0.063	0.943	0.013	0.988

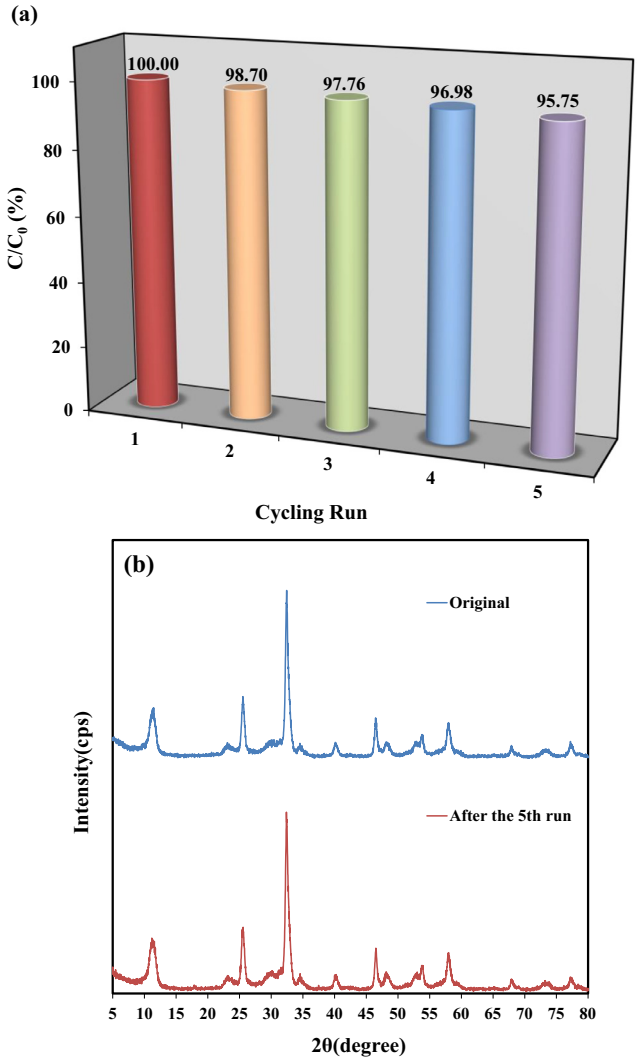

Fig. 9. (a) Cycling runs in the photocatalytic degradation of SA in the presence of BiOCl/BiOBr/BiOI/GO; (b) XRD of powder sample before and after the degradation reaction.

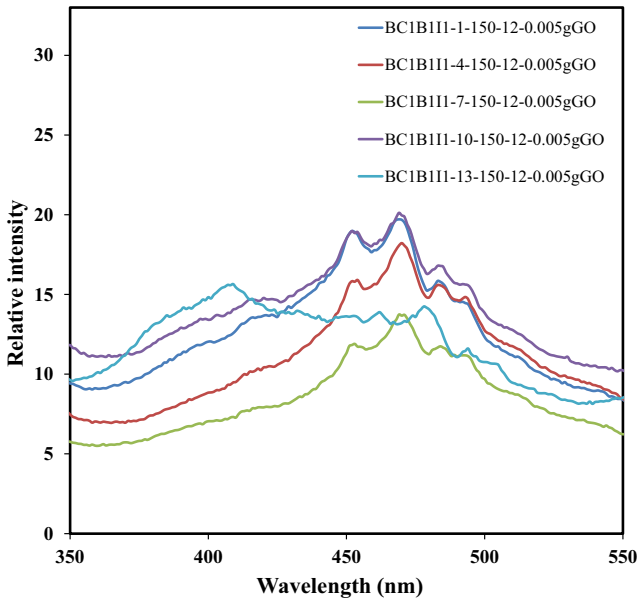

Fig. 10. Photoluminescence spectra of $BiO_xCl_y/BiO_mBr_n/BiO_pI_q$/GO.

confirming the manner through which active $^1O_2$ and ·OH dwelling on the $Bi_2O_2(OH)(NO_3)$ {1 1 1} plane surface engage in rhodamine B, methyl orange, bisphenol A, and tetracycline hydrochloride degradation [61]. Liu et al. determined a superoxide radical acted as the chief reactive species in rhodamine B photodegradation by $Bi_{12}O_{17}Cl_2$ under visible-light irradiation [45], whereas Xia et al. revealed O_2^{-}· and ·OH radicals to be the two major active species throughout the photodegradation reaction by *N*-doped carbon quantum dot (*N*-CQD)-modified $Bi_4O_5I_2$ hollow nanotubes [62]. Wang et al. proposed that ·OH active species were formatted through a multistep reduction of O_2^{-}· radicals [26]. We have suggested that O_2^{-}· oxidation played the key role in CV, phenol, and HBA photodegradation and have argued that the ·OH radical directly resulted from hole oxidation of hydroxide and water [12,13,15,36,39]. Notably, formatting of the HO· radical may only occur through the $e^- \rightarrow O_2^{-}\cdot \rightarrow H_2O_2 \rightarrow$ ·OH pathway, whereas ·OH species are formatted through a multistep O_2^{-}· radical reduction reaction. For the valence band of Bi^{3+}, holes produced by photoexcitation were transferred to the valence band of Bi^{5+} [63]; nevertheless, compared with the OH· radical and OH^- ion, the standard redox potential of $Bi^{3+}$and Bi^{5+} were more negative [64].

These findings indicate that photoformatted holes on the bismuth-oxyhalide surface do not react with OH^-/H_2O species to produce ·OH radical; hence, rhodamine degradation [62] in both species can be attributed to direct chemical reaction with photoformatted $h^{\pm}$ or with an excited electron from an O_2^{-}· radical. Zhu et al. discussed how photocatalytic processes occurring alongside a radical scavenger and nitrogen gas demonstrate that O_2^{-}· active and ·OH radical species are the two major active radicals in photocatalytic processes [65]. According to earlier research [66], the major active species formatted by direct oxidative reactions and photocatalytic processes are $^1O_2$ and ·OH active species, respectively. In visible-light-driven photocatalytic systems, a series of hydroxylated compounds were separated and examined for photocatalytic degradation of crystal violet [25]. Hence, we recommend that the generation of O_2^{-}· radicals is much more feasible than the generation of ·OH radicals.

To further improve our understanding of the photocatalytic activity test, we scavenged for relevant active species in our photocatalytic study by using four quenchers [12,13,36,39,61]. As displayed in Fig. 11, the photocatalytic degradation activity of the BQ quencher exhibited a greater decline than did those of SA, AO, and IPA. This demonstrates that the reactive O_2^{-}· radicals were crucial in HBA photodegradation, whereas the active species of $h^{\pm}$, $^1O_2$, and ·OH $h^{\pm}$ played extremely minor roles, and a multistep reduction of O_2^{-}· radicals formatted the ·OH radicals.

Visible-light irradiation can format these cycles assuming that the light is maintained [27]. The photocatalytic degradation of HBA by the generated active species after multiple cycles can be expressed by Eqns. (27) and (28):

$$HBA + O_2^{-}\cdot \rightarrow \text{photodegraded intermediates} \quad (27)$$

$$HBA + OH\cdot \rightarrow \text{photodegraded intermediates} \quad (28)$$

The O_2^{-}· active species have been formatted by the electron after reaching the conduction band of BiOCl/BiOBr/BiOI/GO, causing HBA degradation. HBA photocatalytic degradation results from BiOCl/BiOBr/BiOI/GO-mediated processes (Fig. 12), and the O_2^{-}· active species causes the reaction of O_2 and electrons photogener-

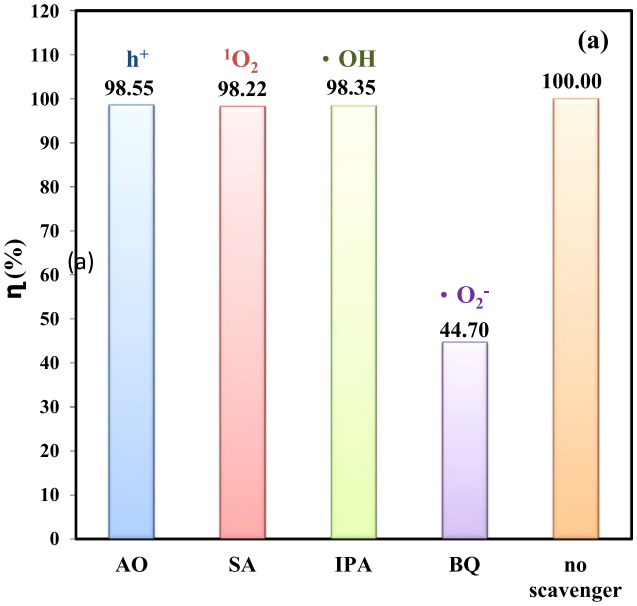

Fig. 11. The HBA concentration during photodegradation as a function of irradiation time observed in BiOCl/BiOBr/BiOI/GO under the addition of different scavengers: SA, IPA, AQ, and BQ with visible light irradiation.

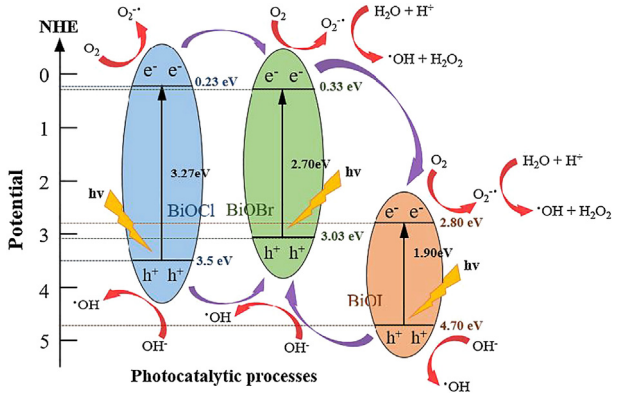

Fig. 12. The band structure diagram of BiOCl/BiOBr/BiOI/GO nanocomposites and the possible charge separation processes.

ated on the surface of the photocatalyst, while the ·OH radical causes reactions of the $O_2^{\cdot-}$ radical with H^+ and/or h^+ with H_2O (or OH^-) [28,31].

4. Conclusions

We prepared a series of quaternary $BiO_xCl_y/BiO_mBr_n/BiO_pI_q$/GO photocatalysts through controlled hydrothermal and template-free synthesis. We designed fine-tuning experiments to examine the various effects of pH and temperature. The photocatalytic performance of BiOCl/BiOBr/BiOI/GO could be attributed to the heterojunction formation between BiOCl, BiOI, BiOI, and GO, which could effectively inhibit photogenerated electron–hole pair recombination. Therefore, the enhanced performance of BiOCl/BiOBr/BiOI/GO can be attributed to the layer structure, heterojunction formation, low-energy band structure, and high BET surface area. In the HBA photodegradation reaction, $O_2^{\cdot-}$ was characterized as the primary active species in the photocatalytic reaction. In the future, the enhancement of visible-light-driven photocatalytic activity clarified herein may be useful for application in organic compound decomposition and environmental remediation.

Acknowledgments

This research was supported by the Ministry of Science and Technology of the Republic of China in Taiwan (MOST-107-2113-M-142 -001). We acknowledge National Taichung University of Education provided instrument for all measurement.

Appendix A. Supplementary material

Supplementary data to this article can be found online at https://doi.org/10.1016/j.jcis.2019.02.067.

References

[1] Y. Qu, X. Duan, Prog. Chem. Soc. Rev. 42 (2013) 2568–2580.
[2] R.L.Z. Hoye, L.C. Lee, R.C. Kurchin, T.N. Huq, K.H.L. Zhang, M. Sponseller, L. Nienhaus, R.E. Brandt, J. Jean, J.A. Polizzotti, A. Kursumovic, M.G. Bawendi, V. Bulovic, V. Stevanovic, T. Buonassisi, J.L. MacManus-Driscoll, Adv. Mater. 29 (2017) 1702176.
[3] D.J. Lapworth, N. Baran, M.E. Stuart, R.S. Ward, Environ. Pollut. 163 (2012) 287–303.
[4] E. Carmona, V. Andreu, Y. Pico, Sci. Total Environ. 484 (2014) 53–63.
[5] L.F. De Tauxe-Wuersch, D. Alencastro, J. Grandjean, Tarradellas, Water Res. 39 (2005) 1761–1772.
[6] Q. Bu, B. Wang, J. Huang, S. Deng, G. Yu, J. Hazard. Mater. 262 (2013) 189–211.
[7] M. Berk, O. Dean, H. Drexhage, J.J. McNeil, S. Moylan, A. O'Neil, M. Maes, BMC Med. 11 (2013) 74.
[8] A.C. Vlot, D.M.A. Dempsey, D.F. Klessig, Ann. Rev. Phytopathol. 47 (2009) 177–206.
[9] A.J. Langstieh, P. Verma, A.K. Thakur, S.S. Chatterjee, V. Kumar, Pharmacologia 5 (2014) 326–338.
[10] E. Brillas, C.A. Martínez-Huitle, Appl. Catal. B: Environ. 166–167 (2015) 603–643.
[11] M. Pelaez, N.T. Nolan, S.C. Pillai, M.K. Seery, P. Falaras, A.G. Kontos, P.S.M. Dunlop, J.W.J. Hamilton, J.A. Byrne, K. O'shea, M.H. Entezari, D.D. Dionysiou, Appl. Catal. B: Environ. 125 (2012) 331–349.
[12] C.W. Siao, H.L. Chen, L.W. Chen, J.L. Chang, T.W. Yeh, C.C. Chen, J. Colloid Interface Sci. 526 (2018) 322–336.
[13] J.Y. Fu, L.W. Chen, Y.M. Dai, F.Y. Liu, S.T. Huang, C.C. Chen, Mol. Catal. 455 (2018) 214–223.
[14] C.C. Chen, J.Y. Fu, J.L. Chang, S.T. Huang, T.W. Yeh, J.T. Hung, P.H. Huang, F.Y. Liu, L.W. Chen, J. Colloid Interface Sci. 532 (2018) 375–386.
[15] C.Y. Wang, X. Zhang, Y.J. Zhang, J.J. Chen, H.Q. Yu, Appl. Catal. B: Environ. 237 (2018) 464–472.
[16] M. Sun, Q. Wei, Y. Shao, B. Du, T. Yan, L. Yan, Appl. Catal. B: Environ. 233 (2018) 250–259.
[17] W. Wang, Q. Zhu, F. Qin, Q. Dai, X. Wang, Chem. Eng. J. 333 (2018) 226–239.
[18] F.Y. Liu, Y.R. Jiang, C.C. Chen, W.W. Lee, Catal. Today 300 (2018) 112–123.
[19] A.H. Lee, Y.C. Wang, C.C. Chen, J. Colloid Interface Sci. 533 (2019) 319–332.
[20] Y.C. Wang, A.H. Lee, C.C. Chen, J. Taiwan Inst. Chem. Eng. 93 (2018) 315–328.
[21] F.Y. Liu, J.H. Lin, Y.M. Dai, C.C. Chen, Catal. Today 314 (2018) 28–41.
[22] M.K. Arfanis, P. Adamou, N.G. Moustakas, T.M. Triantis, P. Falaras, Chem. Eng. J. 310 (2017) 525–536.
[23] B. Réti, Z. Major, D. Szarka, T. Boldizsár, E. Horváth, A. Magrez, L. Forró, A. Dombi, K. Hernádi, J. Mol. Catal. A: Chem. 414 (2016) 140–147.
[24] S.S. Shinde, C.H. Bhosale, K.Y. Rajpure, Mol. J. Catal. A: Chem. 347 (2011) 65–72.
[25] Y.R. Jiang, H.P. Lin, W.H. Chung, Y.M. Dai, W.Y. Lin, C.C. Chen, J. Hazard. Mater. 283 (2015) 787–805.
[26] J. Wang, Y. Yu, L. Zhang, Appl. Catal. B: Environ. 136–137 (2013) 112–121.
[27] W.W. Lee, C.S. Lu, C.W. Chuang, Y.J. Chen, J.Y. Fu, C.W. Siao, C.C. Chen, RSC Adv. 5 (2015) 23450–23463.
[28] S.Y. Chou, C.C. Chen, L.W. Chen, Y.M. Dai, J.H. Lin, W.W. Lee, RSC Adv. 6 (2016) 33478–33491.
[29] K.L. Li, W.W. Lee, C.S. Lu, Y.M. Dai, S.Y. Chou, M.C. Wang, C.C. Chen, J. Taiwan Inst. Chem. Eng. 45 (2014) 2688–2697.
[30] H.L. Chen, W.W. Lee, W.H. Chung, Y.J. Chen, Y.R. Jiang, H.P. Lin, W.Y. Lin, C.C. Chen, J. Taiwan Inst. Chem. Eng. 45 (2014) 1892–1909.
[31] Y.R. Jiang, S.Y. Chou, J.L. Chang, S.T. Huang, H.P. Lin, C.C. Chen, RSC Adv. 5 (2015) 30851–30860.
[32] X. Shi, P. Wang, W. Li, Y. Bai, L. Ye, Appl. Catal. B: Environ. 243 (2019) 322–329.
[33] S. Shenawi-Khalil, V. Uvarov, Y. Kritsman, E. Menes, I. Popov, Y. Sasson, Catal. Commun. 12 (2011) 1136–1141.
[34] X. Xiao, R. Hao, M. Liang, X. Zuo, J. Nan, L. Li, W. Zhang, J. Hazard. Mater. 233–234 (2012) 122–130.
[35] Q. Xiang, J. Yu, M. Jaroniec, Chem. Soc. Rev. 41 (2012) 782–796.
[36] Y.H. Lee, Y.M. Dai, J.Y. Fu, C.C. Chen, Mol. Catal. 432 (2017) 196–209.
[37] H. Liu, W.R. Cao, Y. Su, Z. Chen, Y. Wang, J. Colloid Interface Sci. 398 (2013) 161–167.
[38] S. Song, B. Cheng, N. Wu, A. Meng, S. Cao, J. Yu, Appl. Catal. B: Environ. 181 (2016) 71–78.

[39] S.Y. Chou, W.H. Chung, L.W. Chen, Y.M. Dai, W.Y. Lin, J.H. Lin, C.C. Chen, RSC Adv. 6 (2016) 82743–82758.
[40] X. Xiao, C. Xing, G. He, X. Zuo, J. Nan, L. Wang, Appl. Catal. B: Environ. 148–149 (2014) 154–163.
[41] X. Xiao, R. Hao, X. Zuo, J. Nan, L. Li, W. Zhang, Chem. Eng. J. 209 (2012) 293–300.
[42] H. Liu, Y. Su, Z. Chen, Z. Jin, Y. Wang, J. Mol. Catal. A: Chem. 391 (2014) 175–182.
[43] K.G. Keramidas, G.P. Voutsas, P.I. Rentzeperis, Z. Kristalogr. 205 (1993) 35–40.
[44] E. Wlaźlak, A. Blachecki, M. Bisztyga-Szklarz, S. Klejna, T. Mazur, K. Mech, K. Pilarczyk, D. Przyczyna, M. Suchecki, P. Zawalad, K. Szaciłowski, Chem. Commun. 54 (2018) 12133–12162.
[45] Y. Wang, X. Huang, K. Wang, L. Zhang, B. Wang, Z. Fang, Y. Zhao, F. Gao, P. Liu, W. Feng, J. Mater. Chem. A 6 (2018) 9200–9208.
[46] K.L. Zhang, C.M. Liu, F.Q. Huang, C. Zheng, W.D. Wang, Appl. Catal. B: Environ. 68 (2006) 125–129.
[47] F.A. Bannister, M.H. Hey, Miner. Mag. 24 (1935) 49–58.
[48] J.L. Soubeyroux, S.F. Matar, J.M. Reau, P. Hagenmuller, Solid State Ion. 14 (1984) 337–345.
[49] E. Keller, V. Krämer, M. Schmidt, H. Oppermann, Z. Kristallogr, Cryst. Mater. 217 (2002) 256.
[50] E. Keller, J. Ketterer, V. Krämer, Z. Kristallogr, Cryst. Mater. 216 (2001) 595.
[51] U. Eggenweiler, E. Keller, V. Kramer, Acta Crystallogr. Sect. B: Struct. Sci. 56 (2000) 431–437.
[52] B. Aurivillius, Chem. Scr. 24 (1984) 125–129.
[53] E. Keller, V. Kramer, Acta Crystallogr. Sect. C: Struct. Chem. 63 (2007) i109–i111.
[54] D. Chen, H. Feng, J. Li, Chem. Rev. 112 (2012) 6027–6053.
[55] J. Cao, B.Y. Xu, B.D. Luo, H.L. Lin, S.F. Chen, Catal. Commun. 13 (2011) 63–68.
[56] J. Zhang, F. Shi, J. Lin, D. Chen, J. Gao, Z. Huang, X. Ding, C. Tang, Chem. Mater. 20 (2008) 2937–2941.
[57] F. Dong, Y. Sun, M. Fu, Z. Wu, S.C. Lee, J. Hazard. Mater. 219–220 (2012) 26–34.
[58] C. Nasr, K. Vinodgopal, L. Fisher, S. Hotchandani, A.K. Chattopadhyay, P.V. Kamat, J. Phys. Chem. 100 (1996) 8436–8442.
[59] S.T. Huang, Y.R. Jiang, S.Y. Chou, Y.M. Dai, C.C. Chen, J. Mol. Catal. A: Chem. 391 (2014) 105–120.
[60] N.M. Dimitrijevic, B.K. Vijayan, O.G. Poluektov, T. Rajh, K.A. Gray, H. He, P. Zapol, J. Am. Chem. Soc. 133 (2011) 3964–3971.
[61] Lin Hao, Hongwei Huang, Yuxi Guo, Yihe Zhang, ACS Sustain. Chem. Eng. 6 (2018) 1848–1862.
[62] M. Ji, Y. Liu, J. Di, R. Chen, Z. Chen, J. Xia, H. Li, Appl. Catal. B: Environ. 237 (2018) 1033–1043.
[63] H. Fu, C. Pan, W. Yao, Y. Zhu, J. Phys. Chem. B 109 (2005) 22432–22439.
[64] S. Kim, W. Choi, Kinetics, Environ. Sci. Technol. 36 (2002) 2019–2025.
[65] X. Zhu, J. Zhang, F. Chen, Appl. Catal. B: Environ. 102 (2011) 316–322.
[66] K. Yu, S. Yang, C. Liu, H. Chen, H. Li, C. Sun, S.A. Boyd, Environ. Sci. Technol. 46 (2012) 7318–7326.